

The Four-Quadrant Phase-Mask Coronagraph. II. Simulations

P. RIAUD

LISE, Observatoire de Haute-Provence, F-04870 St Michel l'Observatoire, France; Riaud@obs-hp.fr;
DESPA, Observatoire de Paris-Meudon, 5 Place J. Janssen, F-92195 Meudon, France; Pierre.Riaud@obspm.fr;
and Collège de France, 11 Place M. Berthelot, F-75321 Paris, France

A. BOCCALETTI

Division of Geological and Planetary Sciences, California Institute of Technology, Pasadena, CA 91125; boccalet@gps.caltech.edu

D. ROUAN

DESPA, Observatoire de Paris-Meudon, 5 Place J. Janssen, F-92195 Meudon, France; Daniel.Rouan@obspm.fr

F. LEMARQUIS

Institut Fresnel, Domaine Universitaire de Saint Jérôme, F-13397 Marseille Cedex 20, France; frederic.lemarquis@enspm.u-3mrs.fr

AND

A. LABEYRIE

Observatoire de Haute-Provence, F-04870 St Michel l'Observatoire, France;
and Collège de France, 11 Place M. Berthelot, F-75321 Paris, France; Labeyrie@obs-hp.fr

Received 2001 March 20; accepted 2001 June 12

ABSTRACT. In the first paper in this series, we described the principle of a coronagraph utilizing a four-quadrant phase mask and the results of numerical simulations obtained in the perfect case. In this second paper, we performed additional numerical simulations to assess in more detail the performances and limitations of this coronagraph under real conditions. The effect of geometrical parameters such as shape and size of both the phase mask and the Lyot stop is studied. We also analyze the effect of low- and high-order aberrations generated, for instance, by the atmospheric turbulence. An important issue is the wavelength dependence of the phase mask. We show that the performance decreases rapidly as the spectral bandwidth is increased, and as a consequence, we discuss the manufacturing of achromatized masks using multiple thin films. An optical concept is proposed.

1. INTRODUCTION

In our first paper (Rouan et al. 2000, hereafter Paper I), we presented a coronagraphic concept using a four-quadrant phase mask in the focal plane. Unlike the disk-shaped phase mask (or disk phase-mask coronagraph [DPMC]) described by Roddier & Roddier (1997), the four-quadrant phase mask (FQ-PM) divides the focal plane in four equal areas centered on the optical axis, with two of them providing a π phase shift. This causes destructive interference to occur inside the geometric pupil area. An appropriate Lyot stop is therefore required to block a significant part of the diffracted starlight. This design can, in principle, attenuate a star's halo to the 10^{-8} level, corresponding to 20 mag, at the location of the first Airy ring (Fig. 1). In perfect phasing conditions, the dynamic range then achieved is larger than with a DPMC. Although not achromatic, the nulling performance of the FQ-PM and its behavior regarding the tip-tilt errors are quite similar to those achievable with an achromatic interfero-coronagraph (AIC) (Gay & Rabbia 1996; Baudoz et al. 2000a,

2000b). Under atmospheric turbulence partially corrected with an adaptive optics system, the detection threshold for detecting a faint companion becomes 8–10 mag in contrast in the very close vicinity of the Airy peak ($\sim 3\lambda/D$; see the two simulations' results in Paper I). To improve the rejection rate in very good seeing conditions, the residual speckle pattern can be partly removed by subtracting each pair of quadrants. Finally, we concluded that the capability of the FQ-PM is very promising with regard to the detection of exoplanets in space conditions where the speckle noise is less of a limiting factor and when phase errors are small.

In the § 2 of this paper, we present more detailed numerical simulations which allow us to assess the effect of internal (size of the mask and the stop) and external parameters (low- and high-order aberrations, spectral bandwidth). In § 3 we discuss the use of a large bandwidth with regard to the problem of wavelength dependence, and then we propose a solution to make the π phase shift achromatic over a broad spectral band.

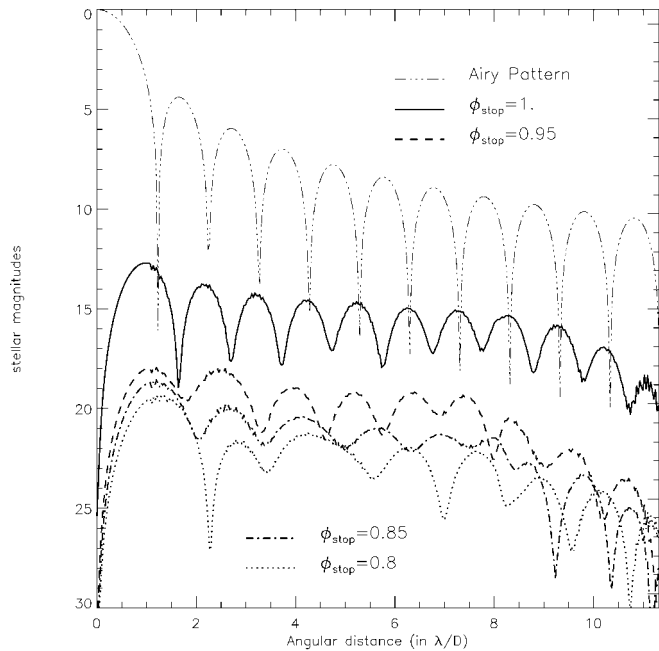


FIG. 1.—Azimuthally averaged coronagraphic intensity profiles obtained with an FQ-PM using four different Lyot stops ranging from 0.8 (*dotted line*) to 1 (*solid line*) times the geometric pupil diameter. We can notice different rejection factors for four Lyot stops and the important gain between 1 and 0.95 (*dashed line*).

2. NUMERICAL SIMULATIONS IN REAL OBSERVING CONDITIONS

2.1. Internal Parameters

Ideally, the mask has to extend across the entire field of view to provide a perfect balancing of the flux in each quadrant, but in practice the size of the mask is finite. Numerical simulations have shown that the optimal sizes of the four-quadrant phase mask and the Lyot stop are closely related. If the field size corresponding to the size of the phase mask is made too small, the intensity at the edges of the relayed pupil becomes larger, and a smaller Lyot stop is required. Figure 2 shows the loss of nulling, compared to the theoretical rejection rate (Fig. 1) as a function of the field size, for four different sizes of the Lyot stop. With a stop size amounting to 95% of the geometric pupil diameter, the mask diameter has to be at least $\approx 32\lambda/D$ to avoid a loss of cancellation.

The pupil shape is another critical parameter with any kind of coronagraphic technique. In Figure 3a, we have quantified the effect of a central obscuration in the entrance aperture. The central obscuration tends to degrade the nulling performance since it diffracts a significant part of the starlight which reappears in the relayed pupil. Diffraction from the inner edge of the pupil has a wider spatial extent than that from the outer edge and contaminates the whole pupil. To mitigate this adverse effect, a larger central Lyot stop is required, but this would affect the intensity and resolution in the image of circumstellar

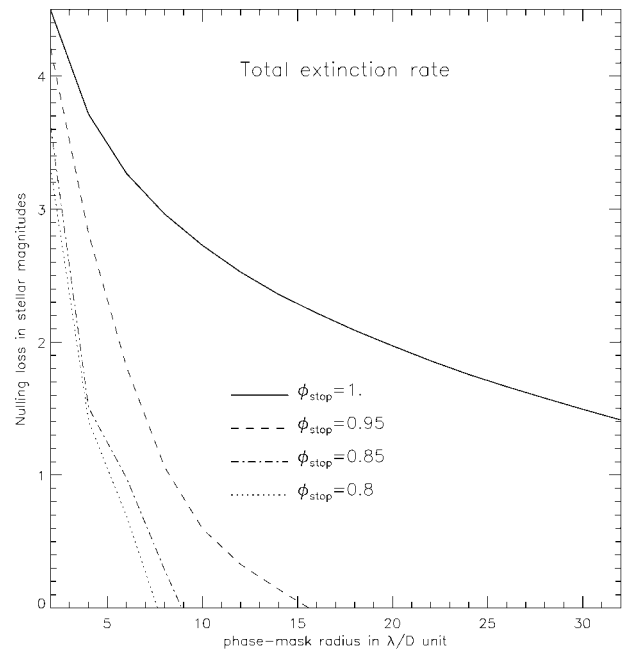


FIG. 2.—Degradation of nulling, given in stellar magnitudes, with respect to the phase mask and Lyot stop radii. The stop size is given in units of the pupil diameter. The nulling degradation is estimated by integrating the residual intensity in the coronagraphic image, relative to a similar integration in the case of an infinite field (Fig. 1). It appears that we can use a phase mask with a diameter of $32\lambda/D$ to have the maximum extinction.

features. Figure 3 gives the attenuation of the starlight (integrated in the coronagraphic image) as a function of the percentage of central obscuration in diameter. The entrance pupil includes a central obscuration with spider arms. The Lyot stop is annular with four different outer diameters [$\phi_{\text{stop}} = \phi_{\text{pup}}(1 - \alpha)$, with $\alpha = 0, 0.05, 0.15, 0.20$]. The corresponding inner diameter is oversized in the same proportion; in other words, $\phi_{\text{out}} = \phi_{\text{pup}}(1 - \alpha)$ and $\phi_{\text{in}} = \phi_{\text{obs}}(1 - \alpha)$. Without central obscuration, the best cancellation is about 18–22 mag (in total intensity) depending on the outer stop's diameter. Then it decreases rapidly with increasing central obscuration, especially in the range 0%–20%, where the dynamic range is lowered by about 8 mag for the smallest Lyot stop. This simulation clearly shows that even a small central obscuration has a significant adverse effect on the coronagraphic capability. In the Figure 3b, the same simulation has been performed with an optimized Lyot stop (simply with the complementary shape of the diffracted light in the pupil). Spiders are added to the previous Lyot stop, and at the inner edge of the pupil, a complementary shape diffracts the starlight. The dynamic range is improved this way by 1–2 mag.

2.2. Attenuation of an Off-Axis Companion

Given the geometry of the phase mask, the intensity of a companion is affected in two different ways in the following

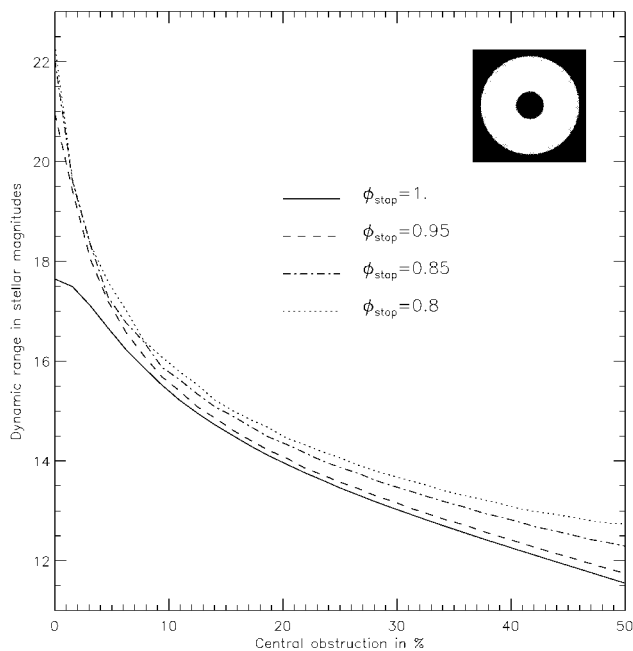


FIG. 3a

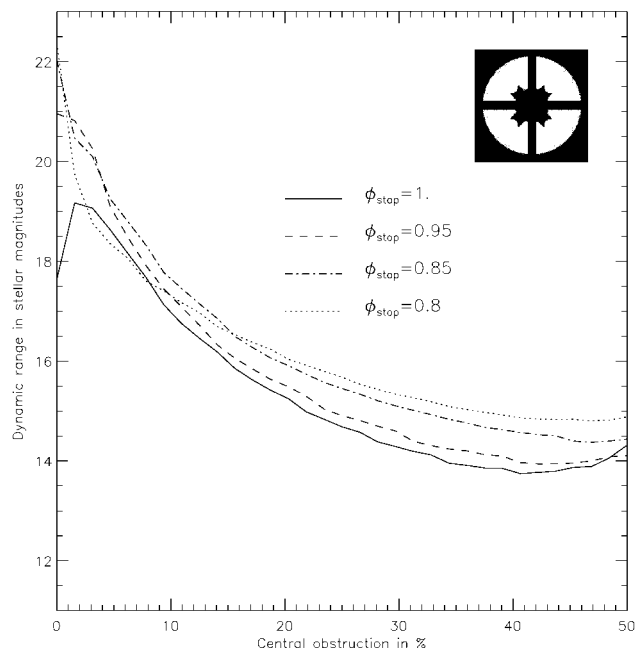


FIG. 3b

FIG. 3.—(a) Effect of a central obscuration. The entrance pupil includes a central obscuration (0%–50%) and spider arms. The Lyot stop is a ring with an outer diameter ϕ_{stop} , and the inner diameter is equal to the central obscuration plus $1/\phi_{\text{stop}}$ in units of the pupil size. (b) Same as Fig. 3a, but with a Lyot stop optimized by thresholding the intensity in the relayed pupil. The dynamic range with an optimized Lyot stop is improved by a factor of 1–2 mag.

cases: (1) If the companion is too close to the center of the phase mask, its image is partially confused with the star's image. Then a significant part of the companion intensity is canceled by the coronagraph. (2) If the companion lies too far from a mask axis, then the π phase shift between the adjacent quadrants produces a partial cancellation of this feature.

These undesirable effects are assessed in Figures 4a and 4b. Figure 4a gives the extinction rate of a companion located at 45° from the x -axis as a function of the distance to the field. The attenuation of the companion is relatively low (<1 mag) when the angular separation is λ/D and decreases to a few tenths of a magnitude for $3\lambda/D$. Therefore, the FQ-PM retains the high angular resolution provided by the full aperture and is able to discriminate the closest stellar companions. As a consequence, the FQ-PM is also very sensitive to guiding errors, as pointed out in Paper I.

Figure 4b shows the extinction of a companion crossing the x -axis and assumed to be far enough from the mask center ($>10\lambda/D$) to avoid the former effect. Although the extinction is almost zero at a distance larger than λ/D from the x -axis, it increases quickly when the companion reaches the transition between two quadrants, depending on the stop diameter. With a stop of 85% of the pupil size, the maximum attenuation is about 3.7 mag. Nevertheless, the companion cannot be completely canceled when it lies along an axis, but the detection may fail if the sensitivity is too poor. A two-quadrant design

is therefore unsuccessful at attenuating the starlight down to the level of extrasolar planets.

2.3. Low-Order Aberrations and Atmospheric Turbulence

In Paper I we studied the effect of the simplest aberration: the tip-tilt of the wavefront. We found that the extinction efficiency is degraded from 20 to 7 mag in the first Airy ring for a residual tip-tilt of $0.088\lambda/D$. The nulling performance decreases as the square of the amplitude of the guiding error (see Fig. 5 of Paper I). In addition, the loss of attenuation is lower in the halo than in the central peak. This is a favorable condition for detecting surrounding faint stellar material. The loss of cancellation in the halo is less than 5 mag for a pointing error of 2% of the angular resolution. The tip-tilt is the most limiting low-order aberration, but the FQ-PM seems to be less affected than other coronagraphic techniques (see Fig. 4b of Paper I). The simulation results obtained for the tip-tilt are also applicable for a resolved star, since it can be considered as a sum of shifted point sources. Note that the Lyot coronagraph (Lyot 1939) is quite insensitive to tip-tilt errors since the opaque mask is much larger than the Airy peak ($>3\lambda/D$). In the current design, the influence of tip-tilt errors can be slightly reduced by adding to the FQ-PM an amplitude mask as in the case of Lyot coronagraphy but considerably smaller. Assuming a tip-tilt of $0.2\lambda/D$ rms, a modest gain of 0.85 mag has been reached

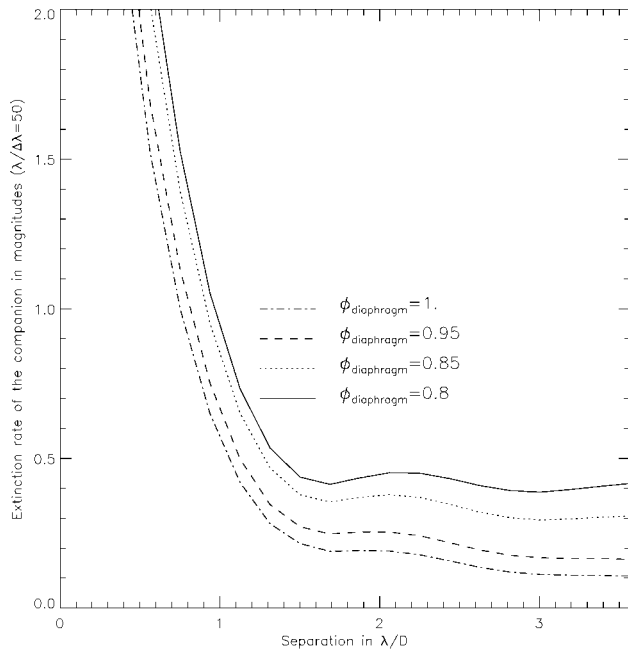


FIG. 4a

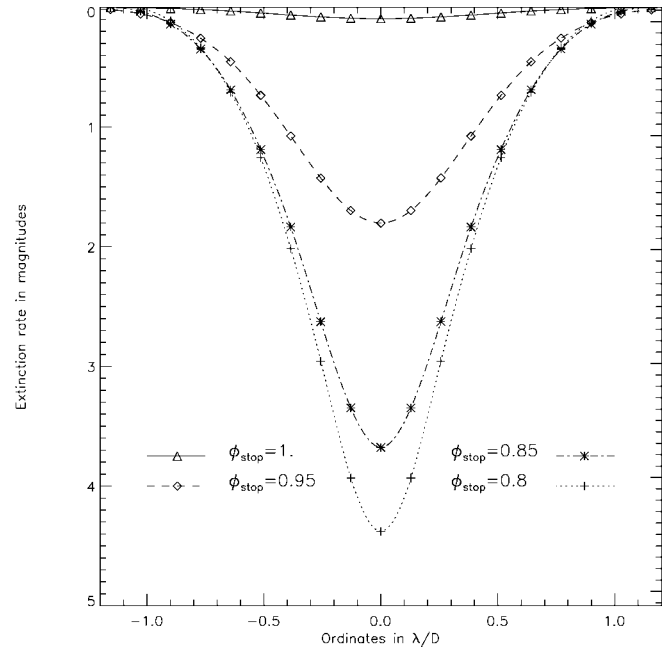


FIG. 4b

FIG. 4.—(a) Attenuation of a stellar companion located at 45° from the x -axis as a function of its distance to the mask center. (b) Attenuation of a companion moving along the y -axis. In each case the simulation is performed for four sizes of the Lyot stop and assuming a monochromatic Airy pattern. The difference between each curve is only the difference for each surface covered by the Lyot stop.

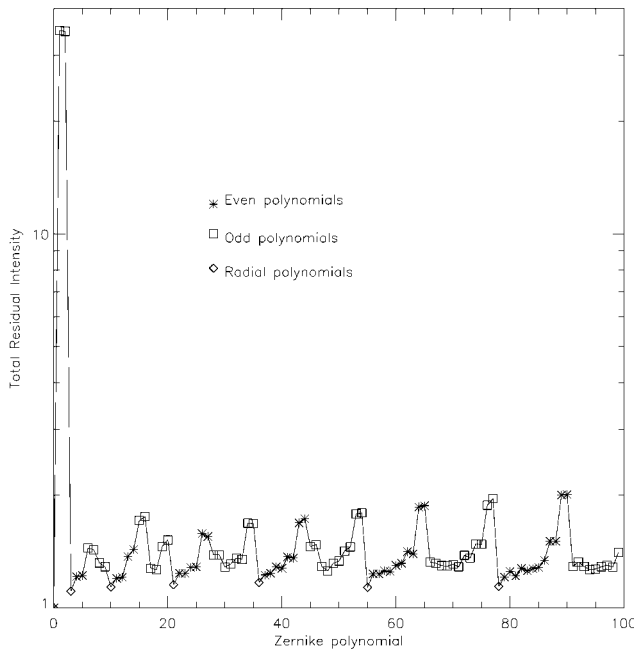


FIG. 5.—Residual intensity in the coronagraphic plane showing the contribution of the Zernike polynomials from Z1 to Z100. We also plot the even polynomials (stars), odd polynomials (squares), and radial polynomials (diamonds, azimuthal order = 0).

with an FQ-PM including a central Lyot mask of $0.09\lambda/D$ in diameter.

To investigate the relative contribution of several aberrations, we compute the FQ-PM image of the first 100 Zernike polynomials. Figure 5 shows the residual intensity in the coronagraphic image for each Zernike polynomial normalized to the residual intensity of a perfect point-spread function (PSF). Although we expected a systematic smaller residual for even polynomials (because they fit the FQ-PM symmetry), Figure 5 shows a more complicated rule which depends both on the radial and azimuthal order. First of all, we found that the tip-tilt (Z2 and Z3) exhibits the largest residual about 20 times higher relative to the other polynomials. Furthermore, for a given radial order, the residual intensity increases with the azimuthal order. Therefore, the zero azimuthal order polynomials (Z1, Z4, Z11, Z22, Z37, Z56, Z79) give the minima (almost constant value). As a result, we observed a pseudoperiodic behavior between two minima. Finally, we also found that the peak-to-valley ratio of a period increases with the radial order. Indeed, as the aberration becomes more complex, the intensity is smeared in a larger area around the PSF core and the phase mask performs a lower attenuation.

Finally, we investigated the effect of atmospheric phase disturbance. Random phase screens corrected with an adaptive optics (AO) system have been generated across the pupil using a Kolmogorov spectrum, for which the power of low spatial frequencies is attenuated to a constant value up to a cutoff

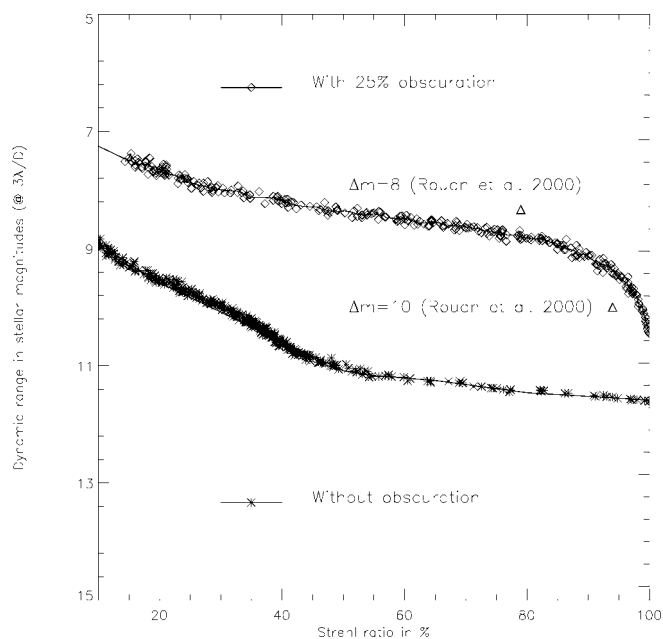


FIG. 6.—Dynamic range in the coronagraphic plane in stellar magnitudes for two cases. *Top*: With 25% central obscuration. *Bottom*: Without central obscuration. Each point is an average of 20 AO-compensated patterns with a Kolmogorov spectrum attenuated below the cutoff frequency. The largest Strehl ratio is about 96%, which is not sufficient to achieve the best extinction (22 mag with no phase errors). If we get rid of the photon noise, the detection of faint companions under atmospheric seeing is mainly limited by the speckle noise (basically proportional to the number of frames). For instance, if the number of frames is increased to 2000, the gain in magnitude is 2.5. The dynamic range would actually greatly improve between 96% and 100%. These simulations are performed with a Lyot stop that is 0.85 times the geometric pupil diameter.

frequency defined by the spacing of the interactuators. Short exposures are derived from each phase map and are co-added to provide the long-exposure coronagraphic image. The resulting Strehl ratio (SR) depends on the turbulence parameters (r_0 , amplitude of the phase defects, and number of actuators). The wavefront has no temporal coherence since the phase screen is entirely updated for each short exposure, and as a result, the speckle halo is more efficiently smoothed than in a real case. Furthermore, quasi-static aberrations downstream the AO system are not considered here. From this series of simulations we derived the dynamic range at $3\lambda/D$ plotted in Figure 6 versus the Strehl ratio. Strehl ratios of 10%–96% have been generated for a full circular aperture and in the case of a 25% central obscuration.

With a full circular aperture, the dynamic range increases from 9 to 11 mag for $10\% < SR < 50\%$ and then becomes quite stable for higher SR. At $SR = 96\%$, the dynamic is only 11.5 mag instead of 22 mag as obtained without phase errors. This large difference is mainly explained by the residual tip-tilt, which exhibits a quadratic dependence (see Fig. 5 of Paper I). As soon as a central obscuration is considered, the dynamic

TABLE 1
MAXIMUM GAIN IN MAGNITUDES WITH SECOND
CORRECTION OF TIP-TILT

RESIDUAL TIP-TILT ERROR AFTER AO (λ/D rms Error in %)	ACCURACY OF FINE TIP-TILT COMPENSATION IN λ/D		
	0.5%	1%	3%
0.2	8	6.5	4.1
0.1	6.5	5	2.6

range is lowered by 2–3.5 mag, as explained in § 2.1. The dynamic range increases slowly to 8.5 mag for $SR < 80\%$ and improves rapidly for $SR > 90\%$ 2 mag for $SR = 96\%$, for instance. The FQ-PM capability is therefore much more affected by the image quality when the pupil features a central obscuration. Since the residual star motion is the major source of degradation, it would be desirable to implement a second stage of tip-tilt correction in the next generation of high-contrast coronagraphs. In this regard, we have estimated the dynamical range with a fine tip-tilt compensation. The gain with respect to Figure 6 is shown in Figures 7a and 7b, respectively, with and without central obscuration. In this case, the PSFs are simply recentered and the tip-tilt accuracy turns out to be improved to $3\%(\lambda/D)$ rms. As expected from the results of Figure 6, the maximum gain (1.5 mag at best) is achieved for $SR < 50$ with a full aperture and around $SR \approx 80\%$ with central obscuration. In the former case, no improvement is noticed above $SR = 60\%$; in the latter, a significant gain is achieved progressively from $SR = 20\%$ to 80% and decreases rapidly since other kinds of aberrations (coma and trifoil, for instance) become dominant at high Strehl ratio. Table 1 gives the maximum gain achieved when the accuracy of fine tip-tilt compensation is $0.5\%(\lambda/D)$, $1\%(\lambda/D)$, and $3\%(\lambda/D)$ rms of the residual AO tip-tilt by direct centroid correction on this second stage.

3. WAVELENGTH DEPENDENCE

3.1. The Monochromatic Case

For a monochromatic phase mask obtained with a thin film of optical index n , the phase retardation is

$$\phi = 2\pi(n - n')e/\lambda,$$

with e the thickness of the layer and n' the optical index of the air. Therefore, the phase shift depends on the wavelength, but the FQ-PM does not have the added difficulty met by the DPMC, where the mask size has to vary in proportion to wavelength.

We have investigated the effect of several spectral bandwidths (from $\Delta\lambda = 5$ nm to $\Delta\lambda = 100$ nm) on a monochromatic FQ-PM (made with a single layer) for both the halo and the peak in the coronagraphic image. Results are displayed in

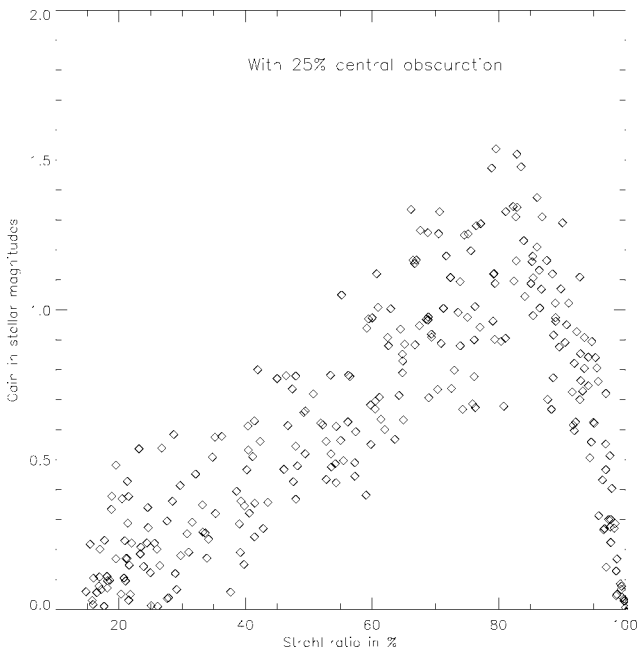


FIG. 7a

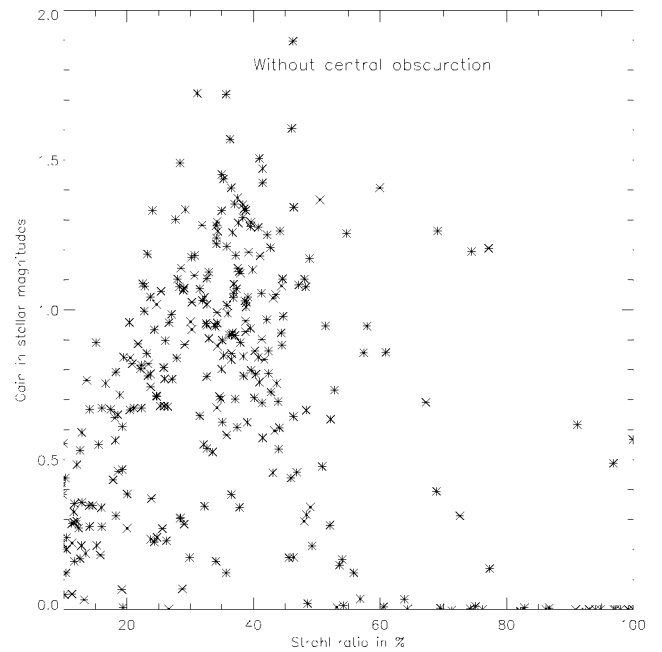


FIG. 7b

FIG. 7.—The contribution of high-order Zernike polynomials. We have removed the tip-tilt contribution by centering the Airy pattern. (a) The gain on the maximum of extinction with 25% central obscuration. (b) The gain on the maximum of extinction without central obscuration. These figures especially show the noise of the tip-tilt correction (here $0.03\lambda/D$).

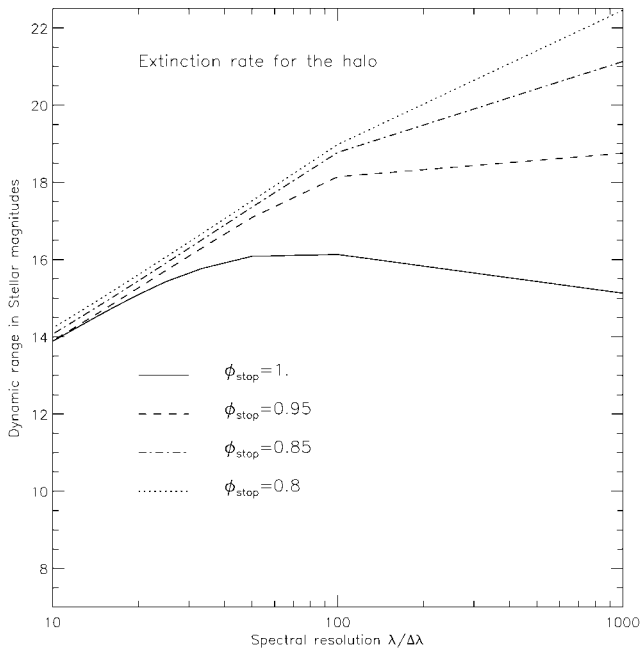


FIG. 8a

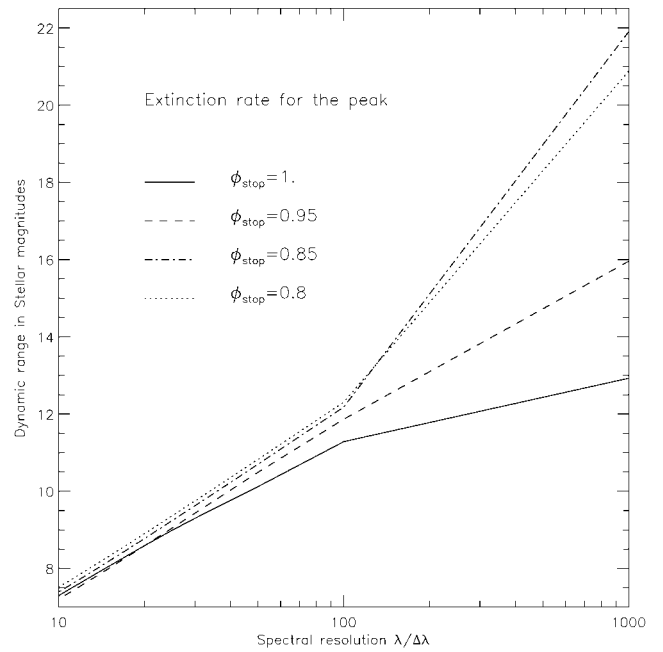


FIG. 8b

FIG. 8.—Dynamic range for (a) the halo and for (b) the peak as a function of the spectral resolution, for four sizes of the Lyot stop and without central obscuration. Panels a and b are applicable for companions farther and closer than $2\lambda/D$, respectively.

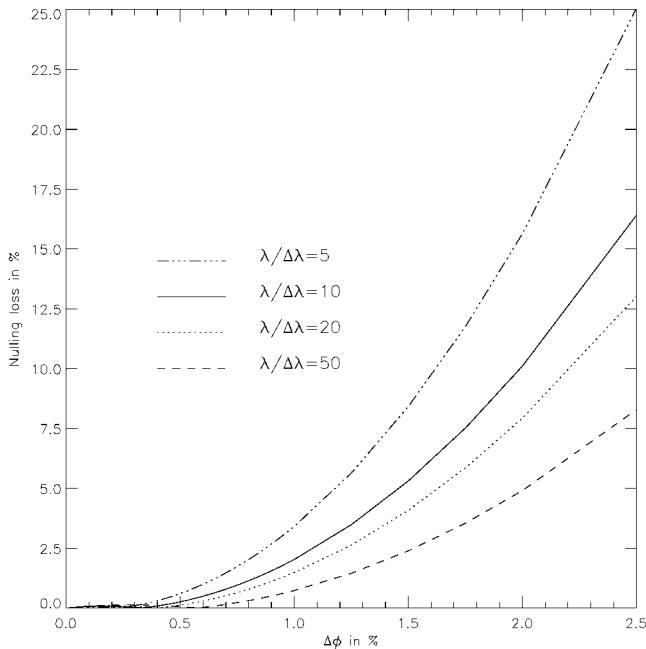


FIG. 9.—Loss of extinction introduced by a phase shift $\pi + \Delta\phi$ (assuming a uniform phase defect) for several spectral resolutions. The nulling loss is small (<25%) even for large spectral bandwidth ($\lambda/\Delta\lambda = 5$) (simulations performed with a monochromatic phase mask).

Figure 8. Here again, the halo is less affected than the peak when the spectral bandwidth is increased.

The dynamic range variation is linear in magnitude with respect to the spectral resolution and features a changing of slope for $R = 100$. The largest value is achieved obviously in monochromatic light (22 mag at best, depending on the Lyot stop) and is lowered to 14 mag in the halo and 8 mag in the peak when the spectral resolution reaches $R = 10$ (typical resolution of broadband filters).

In addition, the size of the Lyot stop has a strong influence on narrow bandwidths and becomes less critical when the spectral band becomes broader ($R < 100$).

Spectral bandwidth is also related to the accuracy of manufacturing. Thickness defects are equivalent to phase defects through the relation $\phi = 2\pi\delta/\lambda$. In Figure 9, the loss of cancellation (in percent) is plotted as a function of a phase defect $\Delta\phi$ given as a percentage of the phase shift ϕ . Assuming a uniform phase defect on the total phase-mask area, the cancellation (ΔI) exhibits a square power law for each spectral bandwidth ($\lambda/\Delta\lambda = 5$ –50). As in the case of tip-tilt errors, this square law was expected since the amplitude of the resulting image is proportional to the phase departure, which is also proportional to the thickness defects. From Figure 9, we derive that $\Delta I \propto x\Delta\phi$ with $x = (\Delta\lambda/\lambda)^{-1/2}$. For instance, with a phase defect of 2.5% ($\equiv 17.4$ nm with a SiO_2 layer), the loss of cancellation is about 8% for the monochromatic case ($\lambda/\Delta\lambda = 50$) and 25% for a larger bandwidth ($\lambda/\Delta\lambda = 5$).

3.2. Achromatization of the Phase Mask

In Paper I, we described the possibility of manufacturing an achromatic phase mask using a stack of thin transparent films. One of us (F. Lemarquis) proposes manufacturing a reflecting phase mask with a high-reflectivity quarter-wave multilayer system using a stacking with a low and high optical indexes. The π phase shift between two quadrants is provided by this layer's structure for the first pair of quadrants and the opposite order for the second pair of quadrants. The alternate high- and low-index layers of quarter-wave thickness are usually represented in the forms “s-HLHL...HLHL-im” for the first pair of quadrants and “s-LHLH...LHLH-im” for the second pair of quadrants, where “H” and “L” symbolize the quarter-wave high- and low-index layers, respectively. The substrate is denoted “s” and the incident medium is denoted “im”; n_H , h_H and n_L , h_L are the indexes of refraction and the physical thicknesses for the two materials. In this scheme, all quadrants have the same reflectivity factors, in the range 700–850 nm (see Fig. 11b).

The effect of the achromatic π phase shift can be easily understood if one considers the simple case of two layers. It is known that there is no phase shift when $n_1 < n_2$ (the first pair of quadrants) and a π phase shift when $n_1 > n_2$ for all wavelengths (the second pair of quadrants).

In your case, a problem appears with the first reflection for the first pair of quadrants. Indeed, this reflection is a π phase shift because the low index $n_L > n_{im}$ if the incident medium is air.

In fact, the perfect π phase shift is obtained when the optical index of incident medium optical index is equal to the index of the quarter-wave mirror $[(n_H n_L)^{1/2}]$. Indeed, the accuracy of the π phase shift provided by the quarter-wave mirror depends on two parameters: first, the index of refraction of the incident medium “im,” and second, the antireflection coating between this incident medium and the quarter-wave mirror. If this coating is a classical broadband antireflection multicoating (BBAR MC) with 0.5% of loss, the phase shift is not accurate enough ($\pi \pm 0.25$ radian). The use of an intermediate fused silica parallel plate ($n_p = 1.453$ at 800 nm) enables one to minimize the difference between the external medium and $(n_H n_L)^{1/2}$ of the quarter-wave mirror. But this contrivance is not sufficient to obtain immediately a phase shift close enough to π , and in this case we have to use BBAR MC, with a mandatory loss lower than 0.1%, in between the quarter-wave mirror and the silica parallel plate. Another solution consists of choosing an intermediate parallel plate with an index near $(n_H n_L)^{1/2}$. Another problem arises when the reflective multilayer mirror is not used at normal incidence: the two polarizations undergo different phase shifts, and this phase error increases with the incidence angle. It turns out that the reflective phase mask must be used close to normal incidence to retain phase errors due to polarization within the phase errors due to imperfect BBAR MC or dispersion effects in the layers.

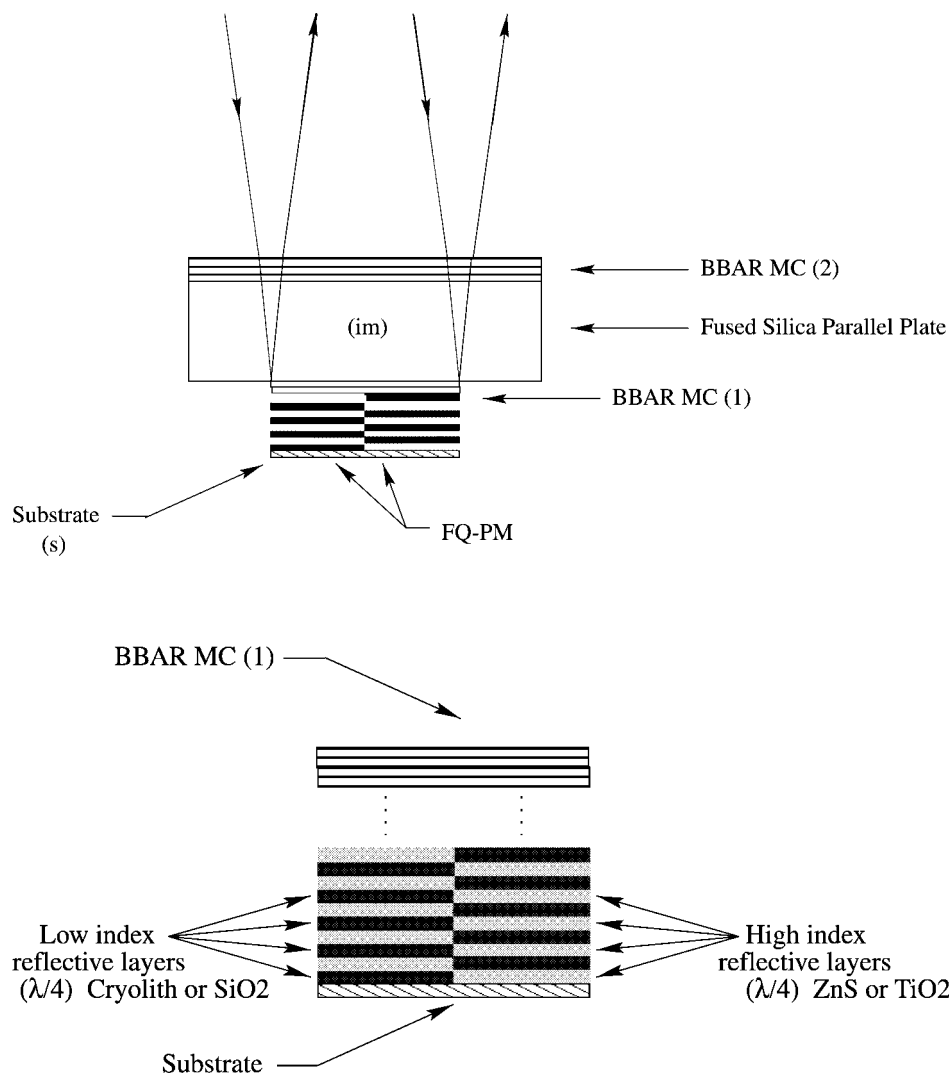


FIG. 10.—Optical scheme for a multilayer phase mask behind a fused silica parallel plate for minimizing the phase shift between the external medium (the parallel plate) and the phase mask.

To optimize an achromatic phase mask in the visible ($\lambda = 700\text{--}850\text{ nm}$) as described above, we adopt an incidence angle of 6° . To obtain a π phase shift with an accuracy of 5.2×10^{-3} , this incidence angle must be smaller than $\approx 10^\circ$. Assuming a central wavelength of 800 nm, the quarter-wave mirror can be made with a high-index material, TiO_2 ($n_H = 2.319$ at 800 nm, $h_H = 86.23\text{ nm}$), and a low-index material, SiO_2 ($n_L = 1.476$ at 800 nm, $h_L = 135.48\text{ nm}$). To achieve a high reflectivity of 99%, 10 layers at least of $\text{TiO}_2\text{-SiO}_2$ must be stacked together.

To minimize the difference in optical index between the fused silica parallel plate and the quarter-wave mirror, we introduce an antireflection coating [BBAR MC(1); Fig. 10] composed of four layers (thickness in parentheses): SiO_2 (39.0 nm), TiO_2 (19.6 nm), SiO_2 (97.0 nm), and TiO_2 (7.3 nm). The second BBAR [BBAR MC(2); Fig. 10] is a classical antireflective

coating between the fused silica parallel plate and the air, optimized for a spectral range of 700–900 nm (see the result in Fig. 11a).

Figure 11a shows the resulting phase shift for the polarizations s and p in the range 700–850 nm. The phase error is about 5.2×10^{-3} radian peak to valley. The reflectivity coefficients are quite good ($>99\%$; see Fig. 11b), but this simulation is optimistic and does not take into account the scattered light in the layers and variation of the thickness of the layers.

A different kind of achromatic concept has been proposed (Abe, Boccaletti, & Vakilli 2001). Instead of a four-quadrant phase mask, it uses a pair of two-quadrant phase masks with variable thickness in two orthogonal directions. The respective efficiencies of these achromatic solutions have to be compared accurately in a laboratory experiment in terms of capability and feasibility.

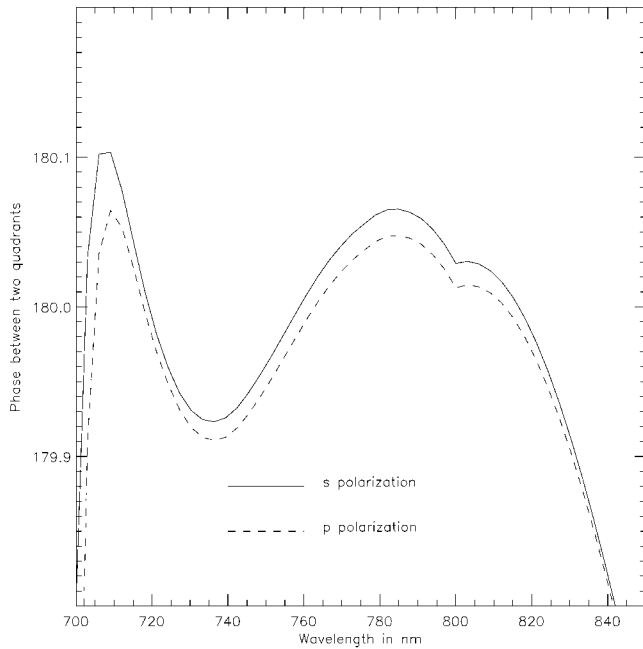


FIG. 11a

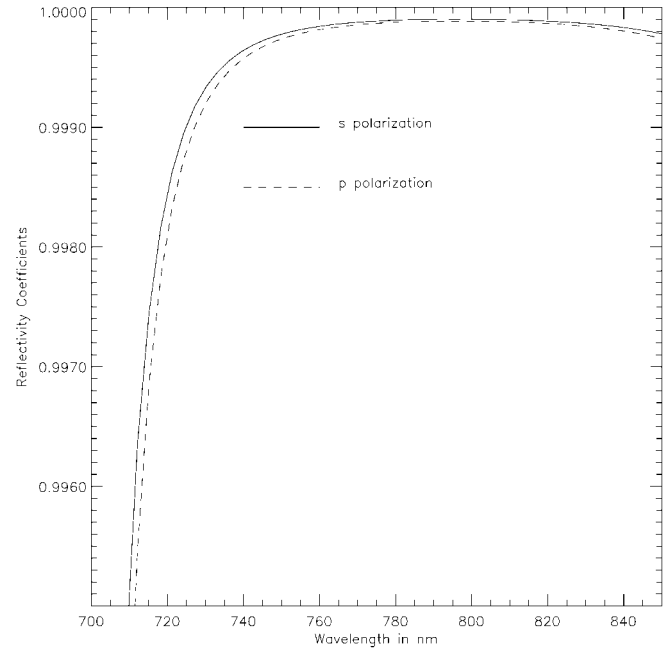


FIG. 11b

FIG. 11.—Simulation result for a multilayer four-quadrant phase mask. (a) Phase shift between two quadrants ($180^{+0.01}_{-0.02}$ PTV for the two polarizations *s* and *p*). (b) Reflectivity coefficients for the quarter-wave phase mask for two polarizations. The results of the calculation take into account the dispersion of the materials.

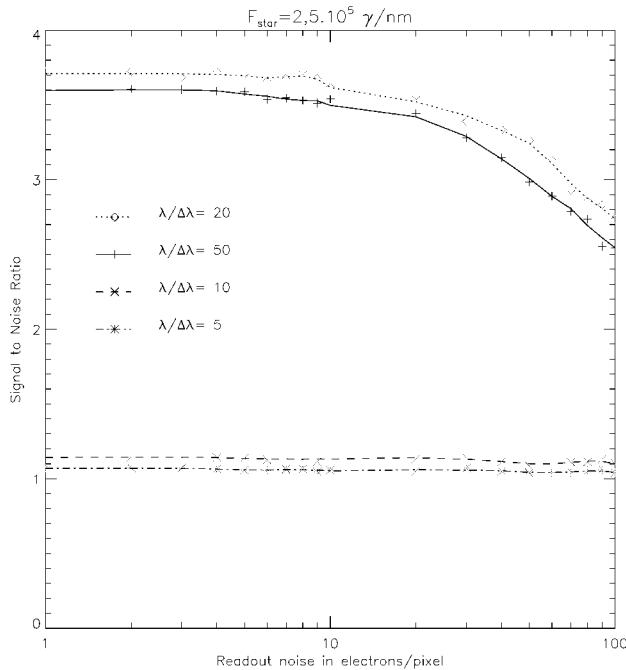


FIG. 12.—Signal-to-noise ratio for the monochromatic phase mask of a companion located at $2.2\lambda/D$ from the star and 15 mag fainter, in four spectral bandwidths assuming photon noise and readout noise. The star flux is 2.5×10^6 photons nm^{-1} , corresponding to 7 mag in the *K* band. We notice a slight signal-to-noise ratio improvement for $\lambda/\Delta\lambda = 20$ compared to the most narrowband phase mask ($\lambda/\Delta\lambda = 50$).

3.3. Photon Noise versus Spectral Bandwidth

Increasing the spectral bandwidth appears of interest for detecting a very faint companion around bright stars. But, as pointed out in § 3.1, the performance of the FQ-PM is wavelength dependent. Thus, a too large bandwidth significantly reduces the contrast in the halo when a monochromatic phase mask is used (see Fig. 8), and the faint companion may be no longer detectable. The choice of the spectral bandwidth is therefore a matter of trade-off between the achievable contrast and the photon noise.

As an example, assuming a 7th magnitude G2 V star (flux $\approx 2.5 \times 10^6$ photons nm^{-1} in the *K* band), numerical simulation has been performed to assess the optimal spectral bandwidth required to detect a companion 15 mag fainter than the star with an angular separation of $2.2\lambda/D$. The signal-to-noise ratio is estimated from the ratio between the intensity of the companion integrated in the Airy peak (with a radius of $1.22\lambda/D$) and the intensity of the background integrated in the same area. This criterion is computed for several spectral resolutions, ranging from 5 to 50 with the FQ-PM being optimized for the central wavelength, various readout noise ($1\text{--}100 e^- \text{pixel}^{-1} \text{frame}^{-1}$), and photon noise. Results are displayed in Figure 12. Using the narrowest bandwidth ($\lambda/\Delta\lambda = 50$), the detection is photon noise limited up to $10 e^- \text{pixel}^{-1} \text{frame}^{-1}$ with a S/N of 3.6. When the readout noise becomes too large, the S/N falls down to the reliable limit of detection (3σ). A modest gain of 3% is achieved when the spectral resolution is decreased to $\lambda/\Delta\lambda = 20$. The capability of detection becomes very poor

($S/N \approx 1$) for $\lambda/\Delta\lambda = 10$ and 5, indicating that there is nothing to gain by increasing the bandwidth at this stage since the signal of the companion is blurred by the Airy patterns corresponding to unextincted λ .

If we compare the S/N obtained in a similar condition but with a supposedly perfectly achromatic FQ-PM, the narrowest bandwidth gives the same result as before, but the S/N is markedly improved with larger bandwidths and reaches 8σ with $\lambda/\Delta\lambda = 5$. Thus, for our multilayer phase mask ($\lambda/\Delta\lambda = 5.4$), the S/N reaches 7σ .

4. CONCLUSION

We have previously shown that the FQ-PM device is able to reach a star/companion ratio of 10^6 – 10^8 in a perfect case

with no phase perturbation. Here we have investigated the loss of cancellation with regard to several parameters in order to have a better understanding of this device in a more realistic case (atmospheric phase disturbance, for instance). We also give an optical solution to achromatize the phase shift. An experiment is currently in progress with a monochromatic phase mask at the Observatoire de Paris–Meudon. We expect a better extinction than with other coronagraphic techniques, but the performance will be constrained by the imperfect thickness of the mask, aberrations of optical components, and homogeneity of the light source. The achromatic device would be directly usable with a good adaptive optics such as PUEO on the Canada-France-Hawaii Telescope or HOKUPA (Guyon et al. 1999) and especially the Nasmyth Adaptive Optics System on the Very Large Telescope (Rousset et al. 2000).

REFERENCES

- Abe, L., Boccaletti, A., & Vakilli, F. 2001, *A&A*, in press
 Baudoz, P., Rabbia, Y., & Gay, J. 2000a, *A&AS*, 141, 319
 Baudoz, P., et al. 2000b, *A&AS*, 145, 341
 Gay, J., & Rabbia, Y. 1996, *CR. Acad. Sci. Paris*, 332, Ser. IIb, 265
 Guyon, O., et al. 1999, *PASP*, 111, 1321
 Lyot, B. 1939, *MNRAS*, 99, 580
 Roddier, F., & Roddier, C. 1997, *PASP*, 109, 815
 Rouan, D., Riaud, P., Boccaletti, A., Clénet, Y., & Labeyrie, A. 2000, *PASP*, 112, 1479 (Paper I)
 Rousset, G., et al. 2000, *Proc. SPIE*, 4007, 72